Observation of quenching-induced magnetic flux trapping using a magnetic field and temperature mapping system

Takafumi Okada,* Eiji Kako, Mika Masuzawa, Hiroshi Sakai, Ryuichi Ueki, and Kensei Umemori

High Energy Accelerator Research Organization (KEK), Tsukuba 305-0801, Japan and SOKENDAI (The Graduate University for Advanced Studies), Tsukuba 305-0801, Japan

Tsuyoshi Tajima

Los Alamos National Laboratory, Los Alamos, New Mexico 87545, USA

(Received 14 December 2021; accepted 22 July 2022; published 29 August 2022)

Highly efficient superconducting radio-frequency cavities exhibit low heat loss and are used as components in accelerators and superconducting devices due to their high Q-values. The precise location of magnetic flux trapping in cavities is necessary to identify its effects on the performance of superconducting cavities. In this study, we report a new combined mapping system to measure the temperature and magnetic field on the equator. The proposed system comprehensively maps local magnetic field changes as magnetic flux trapping due to quenching. Our experimental results show that magnetic flux trapping due to quenching increases the local surface resistance of superconducting cavities at 2 K. Thus, the proposed system elucidates the relationship between local flux trapping due to quenching and surface resistance in superconducting cavities and highlights the effect of quenching on the surface resistance. This system can aid in the development of superconducting cavities with higher Q values.

DOI: 10.1103/PhysRevAccelBeams.25.082002

I. INTRODUCTION

Superconducting radio-frequency (SRF) cavities are high efficiency radio-frequency resonators with low energy loss. They are employed in high energy and high current particle accelerators and are evaluated by the quality factor (Q_0) and accelerating gradient (E_{acc}). High Q_0 values imply smaller power loss (P_0) of the cavity. The Q_0 value can be defined as

$$Q_0 = \frac{\omega U}{P_0}, \tag{1}$$

where ω is the resonant frequency of the cavity, U is the total stored energy in the cavity, and P_0 is the energy dissipation on the wall of the cavity. Since superconducting cavities are constructed from superconducting materials, the energy dissipation is significantly low. P_0 is defined via surface resistance and rf magnetic field on the cavity surface. Surface resistance is typically a few tens of $(\mathrm{n}\Omega)$ at 2 K for 1.3 GHz. However, sustained heat removal is necessary to maintain superconductivity, and cooling is required to dissipate the thermal energy. The main objective of this study is to investigate and improve Q_0 values of superconducting cavities to reduce the heat load in high energy and high current accelerators.

The surface resistance comprises two components: The first is the BCS resistance (R_{BCS}), and the second is the residual resistance (R_{res}) [1]. R_{BCS} is exponentially dependent on the inverse of the temperature, whereas R_{res} exhibits a weak dependence on temperature [2].

One of the causes of the residual resistance is trapped flux in the superconductor. Trapped magnetic flux in the type II superconductor niobium, which is a major material used in superconducting cavities, is quantized. Radio-frequency (rf) waves in the cavity lead to oscillations of the trapped magnetic flux, and the rf power is dissipated on the surface.

The sensitivity of the residual resistance to the magnetic flux is a few tens of $\mathrm{n}\Omega/\mu\mathrm{T}$ for 1.3-GHz Nb cavities [3–7]. Magnetic flux trapping depends on the temperature gradient when the superconductor changes into the superconducting phase [4,8,9]. The cavity geometry and direction of the magnetic field also influence the quantity of trapped magnetic flux [10]. SRF cavities have a curved structure with a size significantly greater than the magnetic quantum flux unit. However, the influence of the magnetic flux on the surface resistance of cavities is observed as a macroscopic behavior of the surface resistance. This issue has been investigated thoroughly in literature [4,8,11,12] based on the global effect on the cavity. Moreover,

*okadat@post.kek.jp

magnetic field and temperature mapping have been successfully used in elucidating the comprehensive geometrical dependency of magnetic flux trapping previously [10,13,14]. Evaluation via the Q_0 value indicates the performance of the efficiency of energy to resonance in the entire cavity. However, the cavity performance is also limited by local phenomena. To this end, magnetic field and temperature mapping can reveal regions in the cavity where the surface resistance due to flux trapping is high.

The contribution of the perpendicular component of the magnetic flux to the surface resistance is larger than that of the parallel component, as demonstrated by the three-dimensional magnetic field and temperature mapping system proposed by Helmholtz-Zentrum Berlin [10,13,15]. SRF cavities capture the magnetic field not only when the cavity is cooled uniformly but also under quenching [16].

When SRF cavities are limited by local quench events on the surface of the cavity, rf power dissipation conducts heat upward at the local surface area. Detailed information on the temperature and magnetic field outside the cavity is important for enhancing the Q_0 value of SRF cavities. In contrast to cooling (from the bottom to the top of the cavity), quenching affects the local distribution of the magnetic field in the rf performance test, where a non-uniform phase transition is observed.

Heating due to quenching leads to large temperature increases on the surface area of the cavity. Even if quenching does not occur, areas with large surface resistance heat up locally due to rf power dissipation. However, this temperature increase is significantly lower than that due to quenching, and temperature mapping systems can measure both heating effects. Furthermore, the trapped magnetic flux is not released when the ambient magnetic field is canceled in the superconducting state. Magnetic field mapping enables the measurement of the change in the ambient magnetic field that is distorted by the trapped magnetic flux on the cavity. However, magnetic flux trapping for SRF cavities due to quenching has not been investigated thoroughly. Observing the distribution of the magnetic field around the cavity can aid in understanding the effect of magnetic flux trapping on the cavity via separation and comparison of the cavity geometry, surface conditions, and material properties. With this motivation, we developed a three-dimensional magnetic field and temperature mapping system with precise angle resolution every 10°.

We describe the magnetic field change around the cavity due to the local trapped magnetic flux caused by several repeated quenches in a uniform vertical magnetic field. Moreover, the proposed system enables observing the local heating and magnetic field distortion.

II. MAGNETIC FIELD AND TEMPERATURE MAPPING SYSTEM

A. Experimental setup

The magnetic field mapping is intended to observe the detailed position and orientation of magnetic flux trapping in SRF cavities. Here, we focused on the magnetic field around the equator of the cavity. Since the cavity has an axially symmetric geometry with the beampipe, the magnetic flux is expelled symmetrically during cooling, provided that the magnetic field is axial to the cavity and the cooldown is uniform. The magnetic field is most enhanced on the equator of the single-cell cavity when the cavity is in the superconducting state, and the uniform magnetic field parallel to the beampipe is applied. However, quenching occurs locally on the cavity surface, and the equatorial region is easily quenched because the rf amplitude peaks at the equator. The remaining ambient magnetic field at the equator has a significant influence on reducing Q_0. The magnetic field and temperature mapping system has been developed to obtain more information on the azimuthal position of the quench at the equator. The experimental setup is explained as follows.

Figure 1 shows the schematic setup of the mapping system for the rf performance test. The boards were aligned to a circular position around the cavity and constrained by aluminum slotted disks for vertical and azimuthal fixing. The outer surfaces of the boards were tied by a copper wire. This system contains 36 printed circuit boards comprising 15 thermometers and 3 magnetic field sensors mounted around the cavity every 10°. The temperature of the outer wall of the cavity is increased by heat transfer inside the cavity wall. Allen Bradley 100 Ω carbon resistors were used as the thermometers [17]. Each board had 15 thermometers, and the total number of thermometers was 540 in the setup. However, some thermometers were not used, because the data acquisition system had limited

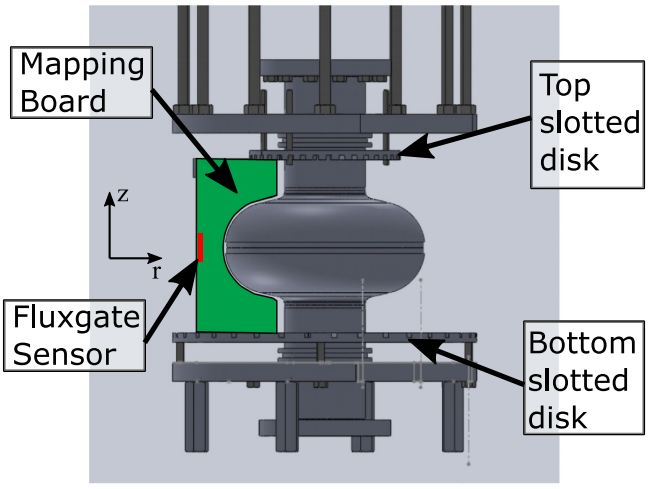

FIG. 1. Schematic model of the mapping board setting for the single cell 1.3-GHz cavity. The cavity was suspended on an aluminum plate jig. The top and bottom slotted disks constrained the mapping boards to fix the vertical axis. The solenoid coil covered the cavity and mapping board to control the vertical axis magnetic field (see Fig. 3). Four fluxgate sensors were mounted every 90° on the outer surface of the boards as a reference value of the magnetic field.

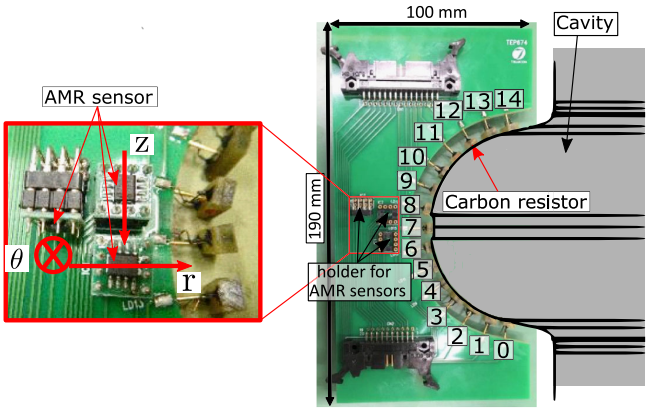

FIG. 2. Magnetic field and temperature mapping board. Fifteen carbon resistors (100 Ω, Allen Bradley) were mounted on the side of the board in contact with the outer wall of the cavity. Numbers show the locations of the surface of the cavity. Three magnetic field sensors were mounted on the center of the board. Each sensitive axis of sensors is z, r, and θ directions, respectively.

channels. The distance between each thermometer on a board was approximately 10 mm. The thermometers covered approximately the entirety of the cavity cell. Three single axis magnetic sensors were mounted on each board to measure the difference in the magnetic field distribution. Sensitec anisotropic magnetoresistive (AMR) sensors AFF755B were used as the magnetic field sensors [13,18]. Figure 2 shows the board containing magnetic field and temperature sensors. The magnetic field sensors were arranged along the z, r, and θ directions perpendicular to each other on the equator of the cavity, as shown in Fig. 2. The AMR sensor positions have 5° offset to the azimuthal angle of the board due to the height of the chip socket.

Connectors were separated on the board for thermometer and magnetic field sensors to avoid interference with the solenoid coil, while controlling the z-direction magnetic field. Output signals were acquired by multiplexers (PXIe-2575) in an NI PXIe system. Since the multiplexers are used for switching sensor channels in the magnetic field and temperature mapping system, the measurement data are not simultaneous.

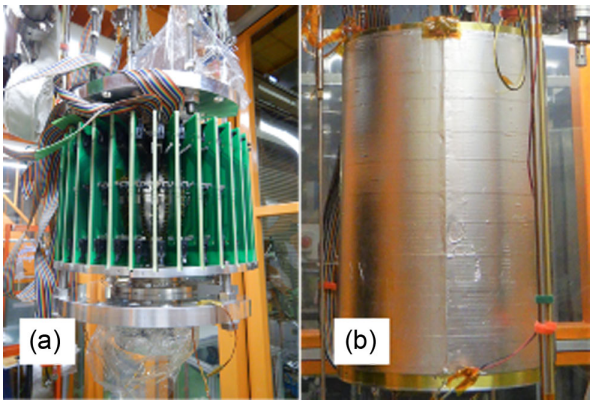

FIG. 3. Photo of the setup of the mapping boards. (a) 36 boards were mounted around the cavity along the circumferential direction. (b) A solenoid coil that controls the ambient z-axis magnetic field covered the mapping boards and cavity.

Fluxgate sensors were also used in the experiment to measure the absolute value of the magnetic field and for calibrating the AMR sensors. For the measurement of Q_0 and E_{acc} in the cavity, four fluxgate magnetometers were attached at the outer side of boards, as shown in Fig. 1. These fluxgate magnetometers were mounted at 0°, 90°, 180°, and 270°. The sensitive axis of all fluxgate magnetometers is the z-direction parallel to the beam axis of the cavity. The ambient magnetic field was controlled by the solenoid coil mounted on the outermost surface of the mapping system. A magnetic shield was installed on the outside of the cryostat. When the current of the solenoid coil was zero, the background magnetic field was less than a few hundred nT.

B. Sensor calibration

The resistors were laminated with G-10 material and housed by epoxy resin for protection and electrical insulation. When mounting the mapping system on the cavity, Apiezon® N-grease was applied on the surface of the thermometers for thermal contact with the surface of the cavity. A pogo stick was mounted on the back of a resistor for contact with the outer wall of the cavity. A constant current of 10 μA was applied to the carbon resistors. The resistance of carbon resistors depends on the temperature. Each carbon resistor had different dependencies on the temperature. Therefore, all carbon resistors need to be calibrated with a reference temperature measured by a silicon diode thermometer during cooling from 4.2 to 2.0 K. The location of the silicon diode thermometer was the equator of the outer cavity wall. The relationship between the resistance and temperature was fitted using the following equation:

$$\log_{10}R + \frac{K_T}{\log_{10}R} = A_T + \frac{B_T}{T}, \tag{2}$$

where R is the resistance of the carbon resistor, T is the temperature, K_T, A_T, and B_T are fitting parameters [19].

The AMR sensor needs to be initialized via magnetization using the flip coil inside the sensor packaging. The initialization process recovers the sensitivity (mV/mT/V) of the AMR sensor, defined as the output voltage per unit magnetic flux density normalized by the power supply voltage. The initial magnetization process needs to be applied to all sensors before cooling. All magnetic field sensors were calibrated as in Ref. [20] at 4.2 K. AMR sensors were calibrated in liquid helium. Solenoid coils applied a magnetic field to the AMR sensors inside the magnetic shield. The range of the magnetic flux density

was $\pm 10\ \mu$T during calibration. The AMR sensor sensitivity was calibrated with the slope of the applied magnetic field that was induced by the solenoid coil and the sensor output. The calibrated sensitivity was $36.84\ \mu\text{V}/\mu\text{T}/\text{V} \times 9\ \text{V} = 331.5\ \mu\text{V}/\mu\text{T}$ at a driven voltage of 9 V. The individual variation was small, at approximately 1%. In this study, the sensitivity of the sensors was $331.5\ \mu\text{V}/\mu\text{T}$.

In the experiments, only the magnetic field sensor along the z-direction was checked for the relative magnetic sensitivity at approximately 20 K during cooling.

III. EXPERIMENTAL RESULTS

A. Procedure and rf measurement results

A 1.3-GHz single cell cavity made of fine-grain niobium was used in our study. The residual resistivity ratio of the niobium sheet is 280–300. The geometry of the cavity was TESLA-like [21], with a geometry factor of 283 Ω. E_p/E_{acc} is 1.87, and besides, B_p/E_{acc} is 4.23 mT/(MV/m).

The cavity was used to study low temperature baking after 30 μm electropolishing and high pressure rinsing. The highest heat treatment temperature of the cavity was 850 °C for 3 h. After studying additional baking, a 20-μm thick layer was removed by electropolishing from the cavity's inner surface.

Finally, thermal treatment was conducted at 75 °C for 4 h and 120 °C for 48 h.

Figure 4 shows the results of the rf performance test in the vertical cryostat. When the ambient magnetic field along the z-direction before phase transition was canceled to values lower than 0.5 μT, the Q_0 value was approximately 2–3 $\times 10^{10}$ in the initial state, as indicated by "Canceled < 0.5 μT" in Fig. 4. The maximum E_{acc} was 27 MV/m, and it was limited by quenching at the upper location of the equator at 20° in the azimuthal angle of the cell, as described later. The experimental procedure to observe the changes in the magnetic field distribution due to local magnetic flux trapping is summarized as follows and in Fig. 5. (1) The ambient magnetic field was canceled using the solenoid coil along the z-direction. The cavity also hardly trapped magnetic flux. This Q_0-E_{acc} curve was the same as the "Full expulsion" result as shown in Fig. 4. (2) Increase coil current to the applied magnetic field in the cavity. The cavity still hardly trapped magnetic flux. (3) The cavity repeated quench events with the magnetic field when the gradient increased, inducing magnetic flux trapping. The Q_0-E_{acc} curve was decreased due to local magnetic flux trapping. (4) Even if the coil current is reduced to cancel the magnetic field, the cavity still trapped the magnetic flux and the Q_0-E_{acc} curve was still decreased. However, if the cavity experiences several quench events without an ambient magnetic field, Q_0-E_{acc} almost recovered as state 1. These steps were repeated with different applied magnetic fields.

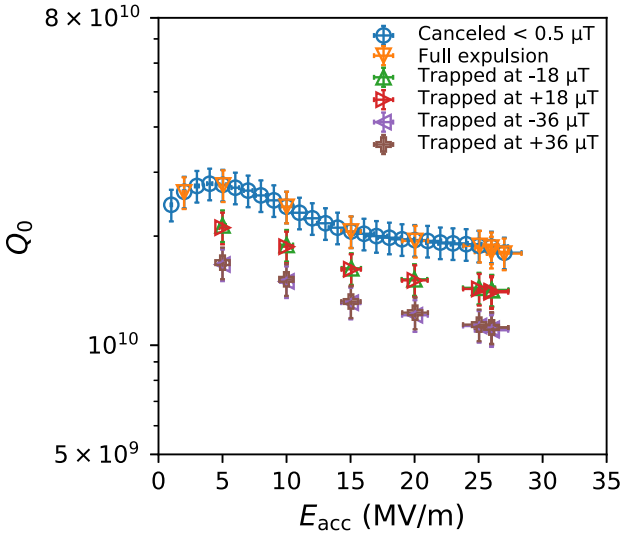

FIG. 4. Results of Q_0-E_{acc} measurements at 2 K. "Full expulsion" which refers to the result of the cavity was not trapped the magnetic flux because the cavity was in the superconducting state. "Trapped at **μT" refers to results with the trapped magnetic flux due to quenching when each magnetic field was applied.

The ambient magnetic field was measured when the cavity was stable in the superconducting state. The difference in the magnetic field between the trapped state and after quenching state implies the distribution of the magnetic field change because the cavity released the trapped magnetic flux. The experimental conditions were presented as Table I.

Figure 4 shows the decreasing Q_0 of the cavity due to magnetic flux trapping. The Q_0 value decreased with the amount of magnetic flux trapped by the cavity.

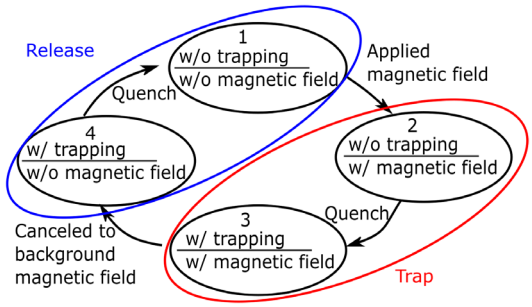

FIG. 5. The sequence of the flux trapping experiment: 1. State demonstrates that the cavity did not trap magnetic flux, and the environment magnetic field was canceled. 2. State demonstrates that the cavity did not trap magnetic flux, and the environment magnetic field was applied. 3. State demonstrates that the cavity trapped magnetic flux, and the environment magnetic field was applied. 4. State demonstrates that the cavity trapped magnetic flux, and the environment magnetic field was canceled. The cavity state can therefore be changed by quenches, and the environment magnetic field was controlled by the solenoid coil current. The arrows show the manipulated coil or quench event between each state.

TABLE I. Table of experiment conditions. Columns are experiment number, cavity state, coil current, applied magnetic flux density, and figure number.

Experiment	Cavity trap state	Coil current ΔI(mA)	B_{ext} (μT)	Figure
No. 1	Trap	100	−18	Figs. 4, 12, and 13
No. 2	Release	100	−18	Figs. 12 and 13
No. 3	Trap	−100	18	Figs. 4, 12, and 13
No. 4	Release	−100	18	Figs. 12 and 13
No. 5	Trap	200	−36	Figs. 4 and 13
No. 6	Release	200	−36	Fig. 13
No. 7	Trap	−200	36	Figs. 4, 7, and 11–13
No. 8	Release	−200	36	Fig. 13

B. Temperature measurements during quenching

The maximum E_{acc} of the cavity was limited by local quench events. To identify the location of the quenches, the rf power was fed to the cavity continuously, and quenches occurred repeatedly more than 3 times. When quenches occurred, the temperature of the outer surface of the cavity was measured using the mapping system. Figure 6 shows the temperature mapping results of heating by quenches. The sensor at $\alpha = 20°$, location 10 was disconnected after cooldown. A smoothing process was applied after measurement to this plot for noise reduction. The temperature measuring area was limited around the heating spot.

The heating spreads for approximately 30° on each side with respect to the center of the maximum temperature position. The temperature increased and reached the peak at a time more than 50 msec, and it required more than 100 msec to recover to 2 K, as shown in the bottom plot of Fig. 6.

After quenching, the cavity trapped magnetic flux. The local magnetic flux trapping causes the local temperature rise. An rf power of 20-sec pulse with a 50% duty cycle was driven in the SRF cavity as an experiment for confirming temperature rises due to magnetic flux trapping. The maximum input rf power was limited so as to avoid quenching in the cavity. Figure 7 shows the heating of the cavity surface in the steady state after quenching with an ambient magnetic field of −36 μT when the pulse peak field was 26 MV/m. When the cavity trapped the magnetic field, the Q_0 value was decreased to approximately 1×10^{10} at 26 MV/m. The local temperature rises returned to the base temperature approximately 2 sec after the rf power was switched off.

C. Magnetic field distribution change due to magnetic flux trapping by quenching

The additional magnetic field after the cavity, which was in the superconducting state, is excluded from the cavity. Figure 8 presents the magnetic field change between the initial state without the external applied magnetic field and the excluded state with the applied magnetic field excited by the solenoid coil current of 10 mA as −1.8 μT. The magnetic fluxgate sensor is compared with magnetic field mapping using AMR sensors. The parameter of the solenoid coil was −0.18 μT/mA. The results show the magnetic flux exclusion of the cavity.

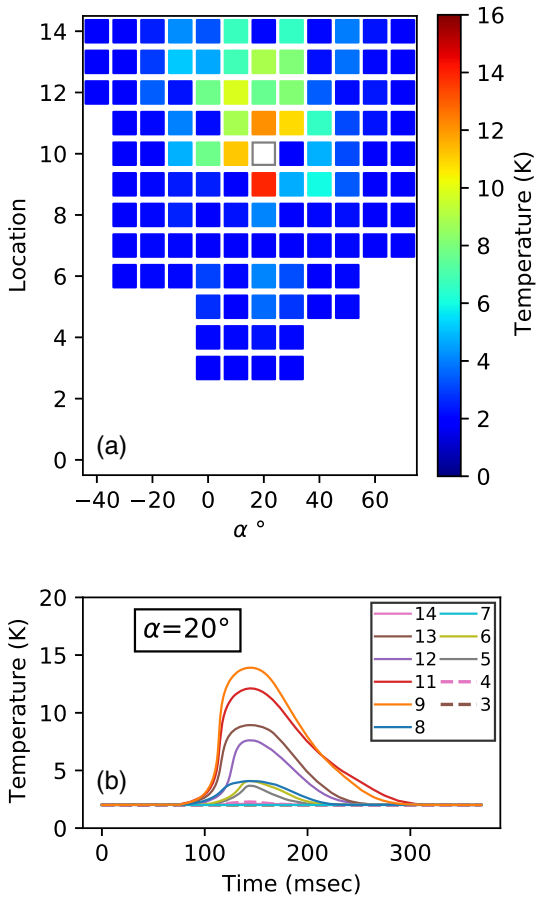

FIG. 6. Temperature rises during repeated quenching at 2 K, as indicated by "canceled < 0.5 μT" in Fig. 4. (a) shows temperature mapping results of the spatial spreading of heating by quenches. (b) shows the time-series measurement of the heating observed at the sensors at the 20° board. (a) and (b) temperature mapping data were measured during regularly repeated quench events so-called self-pulsing quenching. Notably, these temperature mapping results were not simultaneous.

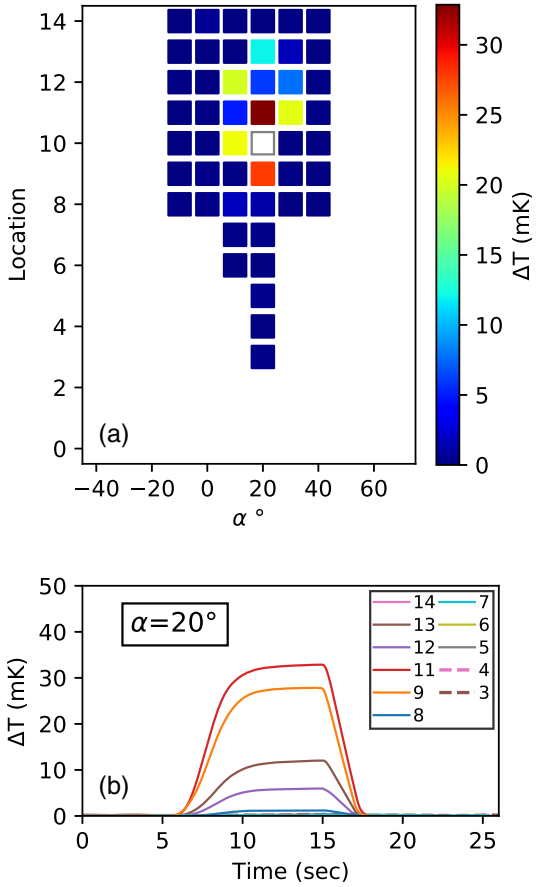

FIG. 7. The temperature rises during heating cycles with a pulsed rf operation. (a) shows temperature mapping results of the spatial spreading of heating by magnetic flux trapping at a local area of the cavity. (b) shows the time-series measurement of the heating observed at the sensors at the 20° board in plot (a). It is noted that these temperature mapping results were not simultaneous because it takes time to switch channels.

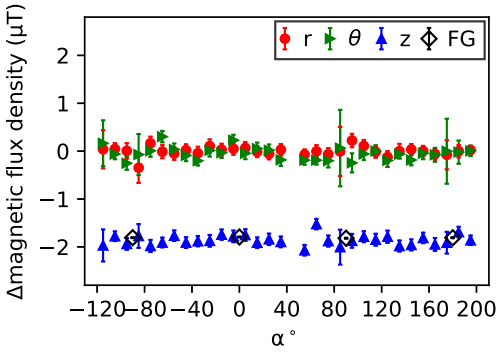

FIG. 8. When the cavity was in the superconducting state, the cavity expelled the applied external magnetic field after phase transition (flux exclusion).

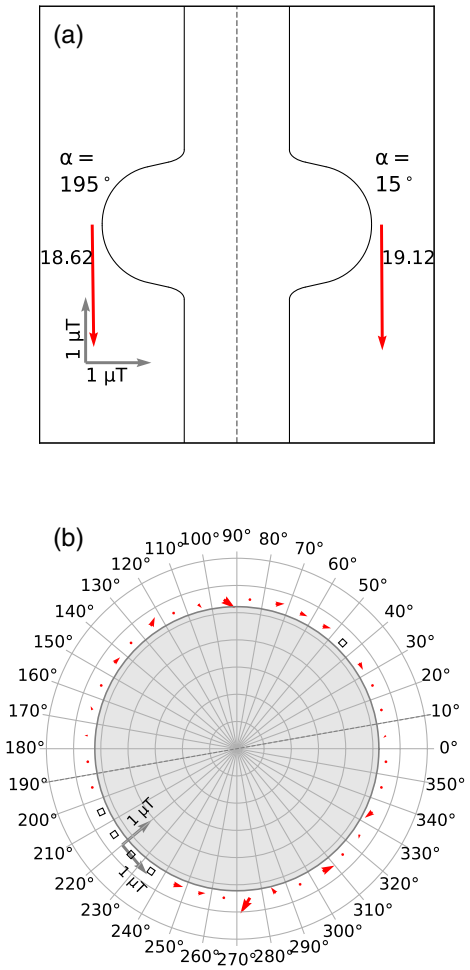

FIG. 9. The magnetic field change during flux exclusion with the applied magnetic field excited by a coil current of 10 mA ($\Delta B \sim -1.8$ μT). (a) shows the z-θ projection and (b) shows the r-θ projection. In the plot (a), the numbers next to the arrows show the absolute value (μT) of magnetic field change.

Figure 9 indicates that the magnetic field was expelled axisymmetrically and uniformly with respect to the z-axis.

In Fig. 4, the Q_0 values were decreased due to magnetic flux trapping from several quenches at 27 MV/m. When the cavity was quenched, a solenoid coil current of 209 mA was applied. Figures 10 and 11 show the magnetic field mapping results when the cavity trapped the magnetic flux locally.

Then, the Q_0 values of the cavity could be recovered by quenching in the zero magnetic field environment.

When the applied magnetic field was changed before quenching, the strength and direction of the trapped magnetic field were also changed. A comparison of the results of the magnetic field mapping is shown as arrows in Fig. 12. Although different magnetic fields were applied, the trapped magnetic field changed toward a specified direction at an approximately 20° azimuthal angle.

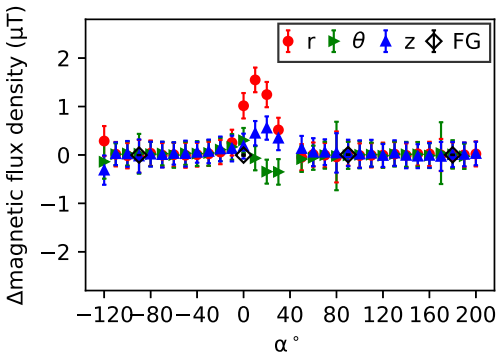

FIG. 10. Magnetic field distribution difference before and after several quenches. When the cavity was quenching, a magnetic field of -18 μT was applied along the z-direction.

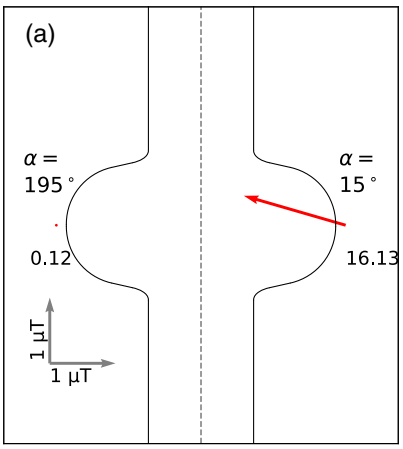

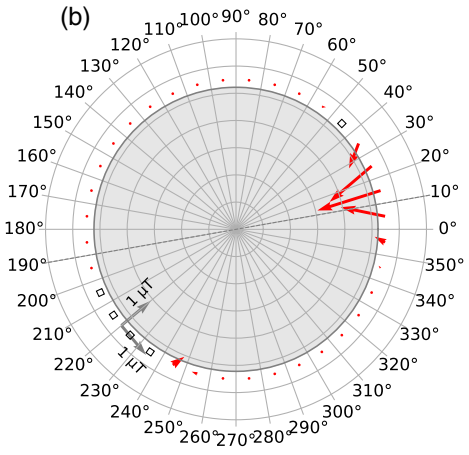

FIG. 11. Example of a 2D image of the change in the magnetic field between, before, and after quenching with a -18 μT magnetic field. (a) shows the z-θ projection and (b) shows the z-θ projection. In the plot (a), the numbers next to the arrows show the absolute value (μT) of magnetic field change.

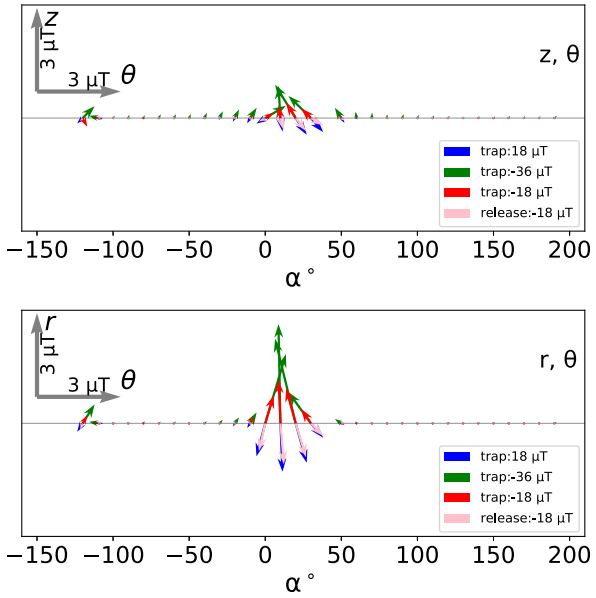

FIG. 12. Comparison of the difference in the magnetic fields before and after quenching with different applied magnetic fields. The top plot shows the z and θ relationship of the change in magnetic fields. The bottom plot shows the r and θ relationship of the change in magnetic field.

The result in Fig. 12 shows the magnetic field change between the cavity trapped magnetic field with an 18-μT applied magnetic field and the cavity released magnetic field due to quenches with zero magnetic field. The magnetic fields in all directions were proportional to the applied magnetic field. An observation of the relation at $\alpha = 15°$ is shown in Fig. 13. The slope differs according to the location and direction, as shown in Fig. 11.

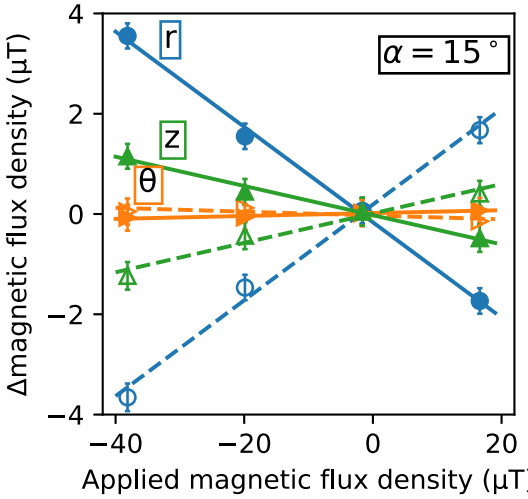

FIG. 13. Linearity of the change in the magnetic field trapping to the applied magnetic field (closed markers) and releasing case (open markers) at 15°. The solid lines denote linear regression.

IV. DISCUSSION

As seen in Figs. 6 and 10, quenching is localized at the upper cell at approximately 20° in the azimuthal angle from the temperature mapping measurements of surface heating. Moreover, the magnetic field mapping results show that the magnetic flux was trapped at the same location.

Quenching generated a localized normal conducting area in the cavity, and the rest of the cavity maintained the superconducting state. The ambient magnetic field distribution changed around the normal conducting area. After quenching, the cavity returned to the superconducting state again. However, the local region trapped the magnetic flux during the phase transition. In this experiment, the cavity trapped magnetic flux sufficiently via multiple quenches, each lasting a few seconds. However, the data acquisition speed was much slower than the time scale of quench dynamics. It was possible to detect the flux trapping phenomenon in the steady state before and after the quench. Moreover, it was difficult to observe the transient state of the magnetic flux trapping into the cavity surface during the quench.

Additionally, field emission and multipacting were not observed at any accelerating gradient. Hence, quenches that limited the cavity performance were caused by surface defects, and the magnetic flux was trapped at that quench location. After magnetic flux trapping, the magnetic flux was fixed at the initial position, even as the accelerating gradient changed. According to these results, it can be considered that several pinning sites for easy trapping of magnetic fluxes might exist inside the cavity wall.

Figure 14 shows the relationship between the surface resistance and absolute strength of the applied magnetic field. For each accelerating gradient, it was found that the surface resistance was proportional to the applied magnetic field.

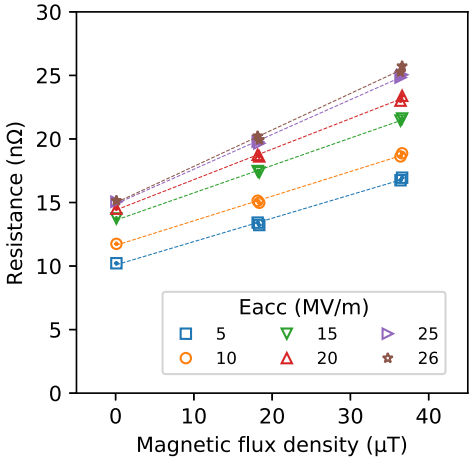

FIG. 14. Relationship between the applied magnetic field and surface resistance of the cavity with locally trapped magnetic flux. The horizontal axis is the absolute strength of the magnetic field and the vertical axis is the surface resistance of the cavity obtained via rf measurement. The surface resistance is proportional to the applied magnetic field at each accelerator gradient.

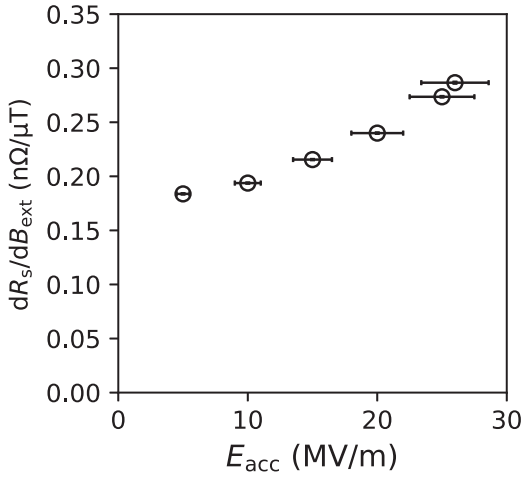

FIG. 15. Slope of surface resistance with applied magnetic field and accelerating gradient.

The surface resistance (R_s) increases with the accelerating gradient (E_{acc}) at the same applied magnetic field (B_{ext}). Figure 15 shows the accelerating gradient dependence of the slope of resistance (dR_s/dB_{ext}), as seen in Fig. 14. It is shown that the slope of the sensitivity of the surface resistance to the magnetic field increases with E_{acc}.

V. CONCLUSION

The magnetic flux trapping caused by quenching and local heating was observed using a magnetic field and temperature mapping system. The magnetic field mapping system focused on the outer equator of the cavity with three axes and revealed the cavity trapped magnetic flux at the quench site by measuring the heating and magnetic field distribution change. The cavity performance was limited by quenching at the local area without multipacting and field emissions. The quench events induced the local entry of the magnetic field due to the ambient magnetic field. The trapped magnetic flux was fixed at the quench location after the entire cavity was recovered to the superconducting state. The influence of local flux trapping on the Q_0 values was proportional to the applied magnetic field with an accelerating gradient. This result shows the relationship between the localized magnetic flux trapping caused by quenching and increasing the local surface resistance of the SRF cavity.

This relation is dependent on the cavity geometry, surface preparation methods, and heat treatment temperature.

In a future study, we will investigate the systematic comparison of the spatial magnetic flux trapping and the change of Q_0 values.

ACKNOWLEDGMENTS

We would like to acknowledge the SRF group for the cavity experiment, and S. Imada, Y. Kikuchi, M. Asano, and H. Yamada for technical support, Dr. H. Ito, H. Araki, Dr. M. Nishiwaki, Dr. P. Pizzol, A. Poudel for discussion, and Y. Kondo for the advice of temperature sensors. This research was partially supported by U.S.-Japan Science and Technology Cooperation Program in High Energy Physics. This research was also partially supported by JSPS Grant-in-Aid for Scientific Research (KAKENHI) Grant No. JP19H04402.

[1] H. Padamsee, J. Knobloch, and T. Hays, *RF Superconductivity for Accelerators* (John Wiley, New York, 1998).

[2] B. Piosczyk, P. Kneisel, O. Stoltz, and J. Halbritter, Investigations of additional losses in superconducting niobium cavities due to frozen-in flux, IEEE Trans. Nucl. Sci. **20**, 108 (1973).

[3] D. Gonnella, J. Kaufman, and M. Liepe, Impact of nitrogen doping of niobium superconducting cavities on the sensitivity of surface resistance to trapped magnetic flux, J. Appl. Phys. **119**, 073904 (2016).

[4] J. M. Vogt, O. Kugeler, and J. Knobloch, Impact of cooldown conditions at T_c on the superconducting rf cavity quality factor, Phys. Rev. ST Accel. Beams **16**, 102002 (2013).

[5] C. Vallet *et al.*, Flux trapping in superconducting cavities, in *Proceedings of the 3rd European Particle Accelerator Conference, EPAC'92, Berlin, Germany* (JACoW, Geneva, 1992), pp. 1295–1298, https://accelconf.web.cern.ch/e92/PDF/EPAC1992_1295.PDF.

[6] G. Ciovati and A. Gurevich, Measurement of rf losses due to trapped flux in a large-grain niobium cavity, in *Proceedings of 13th Workshop on RF Superconductivity, SRF'07, Perking University, Beijing, China* (JACoW, Geneva, 2007), pp. 132–136, https://accelconf.web.cern.ch/srf2007/PAPERS/TUP13.pdf.

[7] P. Dhakal, G. Ciovati, and A. Gurevich, Flux expulsion in niobium superconducting radio-frequency cavities of different purity and essential contributions to the flux sensitivity, Phys. Rev. Accel. Beams **23**, 023102 (2020).

[8] A. Romanenko, A. Grassellino, O. Melnychuk, and D. A. Sergatskov, Dependence of the residual surface resistance of superconducting radio frequency cavities on the cooling dynamics around T_c, J. Appl. Phys. **115**, 184903 (2014).

[9] S. Huang, T. Kubo, and R. L. Geng, Dependence of trapped-flux-induced surface resistance of a large-grain Nb superconducting radio-frequency cavity on spatial temperature gradient during cooldown through T_c, Phys. Rev. Accel. Beams **19**, 082001 (2016).

[10] F. Kramer, O. Kugeler, J.-M. Köszegi, and J. Knobloch, Impact of geometry on flux trapping and the related surface resistance in a superconducting cavity, Phys. Rev. Accel. Beams **23**, 123101 (2020).

[11] T. Kubo, Flux trapping in superconducting accelerating cavities during cooling down with a spatial temperature gradient, Prog. Theor. Exp. Phys. **2016**, 053G01 (2016).

[12] J. Knobloch and H. Padamsee, Flux trapping in niobium cavities during breakdown events, in *Proceedings of the of the 8th Workshop on RF Superconductivity, Abano Terme (Padova), Italy* (JACoW, Geneva, 1997), p. 337, https://accelconf.web.cern.ch/SRF97/papers/srf97b06.pdf.

[13] B. Schmitz, J. Köszegi, K. Alomari, O. Kugeler, and J. Knobloch, Magnetometric mapping of superconducting rf cavities, Rev. Sci. Instrum. **89**, 054706 (2018).

[14] I. P. Parajuli, G. Ciovati, and J. R. Delayen, Magnetic field sensors for detection of trapped flux in superconducting radio frequency cavities, Rev. Sci. Instrum. **92**, 104705 (2021).

[15] D. Longuevergne and A. Miyazaki, Impact of geometry on the magnetic flux trapping of superconducting accelerating cavities, Phys. Rev. Accel. Beams **24**, 083101 (2021).

[16] M. Checchin, M. Martinello, A. Romanenko, A. Grassellino, D. A. Sergatskov, S. Posen, O. Melnychuk, and J. F. Zasadzinski, Quench-Induced Degradation of the Quality Factor in Superconducting Resonators, Phys. Rev. Applied **5**, 044019 (2016).

[17] J. Knobloch, H. Muller, and H. Padamsee, Design of a high speed, high resolution thermometry system for 1.5 GHz superconducting radio frequency cavities, Rev. Sci. Instrum. **65**, 3521 (1994).

[18] AFF755B, Magnetoresistive Field Sensor Sensitec GmbH (2018).

[19] J. R. Clement and E. H. Quinnell, The low temperature characteristics of carbon-composition thermometers, Rev. Sci. Instrum. **23**, 213 (1952).

[20] T. Okada, E. Kako, T. Konomi, M. Masuzawa, H. Sakai, K. Tsuchiya, R. Ueki, K. Umemori, P. Pizzol, A. Poudel, and T. Tajima, Systematic evaluation of magnetic sensitivities of anisotropic magnetoresistive sensors at liquid helium temperature for superconducting cavities, Rev. Sci. Instrum. **92**, 035003 (2021).

[21] E. Kako, H. Hayano, S. Noguchi, N. Ohuchi, M. Satoh, T. Shishido, K. Watanabe, and Y. Yamamoto, Cryomodule tests of four Tesla-like cavities in the Superconducting rf Test Facility at KEK, Phys. Rev. ST Accel. Beams **13**, 041002 (2010).